A Non-Hermitian Moiré Valley Filter

Kai Shao,[1] Hao Geng,[1] Erfu Liu,[1] Jose L. Lado,[2] Wei Chen,[1,*] and D. Y. Xing[1]

[1] *National Laboratory of Solid State Microstructures, School of Physics, and Collaborative Innovation Center of Advanced Microstructures, Nanjing University, Nanjing, 210093, China*

[2] *Department of Applied Physics, Aalto University, 02150 Espoo, Finland*

(Dated: April 19, 2024)

A valley filter capable of generating a valley-polarized current is a crucial element in valleytronics, yet its implementation remains challenging. Here, we propose a valley filter made of a graphene bilayer which exhibits a 1D moiré pattern in the overlapping region of the two layers controlled by heterostrain. In the presence of a lattice modulation between layers, electrons propagating in one layer can have valley-dependent dissipation due to valley asymmetric interlayer coupling, thus giving rise to a valley-polarized current. Such a process can be described by an effective non-Hermitian theory, in which the valley filter is driven by a valley-resolved non-Hermitian skin effect. Nearly 100% valley-polarization can be achieved within a wide parameter range and the functionality of the valley filter is electrically tunable. The non-Hermitian topological scenario of the valley filter ensures high tolerance against imperfections such as disorder and edge defects. Our work opens a new route for efficient and robust valley filters while significantly relaxing the stringent implementation requirements.

Introduction.-Valleytronics [1–4], exploits the valley degree of freedom for electronic information processing and storage similar to the use of spin degree of freedom in spintronics [5]. As the K and K' valleys are distinctly separated in reciprocal space, graphene and other hexagonal 2D materials have become promising candidates for the valleytronic devices. Various valley-resolved phenomena have been explored, including the valley Hall effect [6–9], optical control of valley polarization [10–13], and valley Zeeman effect [14–18]. This demonstrations exemplify the feasibility to manipulate the valley degree of freedom. Just as spin-polarized current serves as a key ingredient in spintronics [5], the implementation of valley-polarized current is a prerequisite for any valleytronic applications. Various proposals have been put forward to generate valley-polarized current in graphene, including using the zeroth mode of the zigzag ribbon [1], line defects [19–21], zero-line modes [22–25], mechanical strain [26–28] and nanobubbles [29]. Despite intense efforts, achieving an ideal valley filter capable of generating fully valley-polarized current with controllable valley polarization remains challenging [3]. Therefore, it is crucial to explore new strategies that can achieve a highly efficient valley filter, and simultaneously, tolerate various device imperfections.

Physical effects that are robust against imperfections are commonly found in systems with nontrivial topological properties. One such example is the chiral edge states of the quantum Hall phase, which are robust to disorder [30]. In Hermitian systems, nonreciprocal transport can only occur at the boundaries of the sample. To achieve unidirectional transport in the bulk, it is necessary to disrupt the Hermiticity of the system [31–33], or turn it open. Recently, great progress has been made in this direction. Unidirectional transport can be achieved inside the bulk, which causes accumulation of states at open boundaries, known as the non-Hermitian skin effect [34–39]. Such nonreciprocal bulk transport also has a topological origin [40–43], the point gap topology of the complex spectrum, indicating its robustness against imperfections. Inspired by the analysis above, a robust valley filter was suggested to be implemented through valley-resolved nonreciprocal transport in the non-Hermitian regime, which can be engineered in mesoscopic electronic systems [44].

In this Letter, we propose a robust valley filter using the 1D moiré pattern formed in a graphene homobilayer, as illustrated in Fig. 1(a), referred to as the moiré valley filter. The setup has an interface structure composed of the upper layer (system S) and the lower layer (reservoir R), along with four terminals (1-4). If layer R is subjected to a uniaxial tension, the coupling between S an R can be valley-dependent. Due to such a lattice modulation, the electrons in S that flow from terminal 1 to 2 initially occupy both valleys and then undergo a valley selective filtering by R, thus generating a valley-polarized current [cf. Fig. 1(a)]. Physically, the valley-dependent coupling with R introduces an effective non-Hermitian self-energy to S, which leads to valley-resolved nonreciprocal transport. Specifically, the electrons in the K (K') valley can only propagate in the x ($-x$) direction, while its propagation in the opposite direction will have a strong decay. The scenario can be interpreted by the valley-resolved complex spectral winding, which induces nonreciprocity within each valley. Such non-Hermitian topological effect enables the valley filter to be resilient against imperfections such as disorder and edge defects, features of major importance towards its practical implementation.

Model.-We take the region S as a zigzag graphene nanoribbon with a width of W_S along the x direction, stacked on top of the R layer with a length of W_R in such a way that their zigzag edges are aligned with each

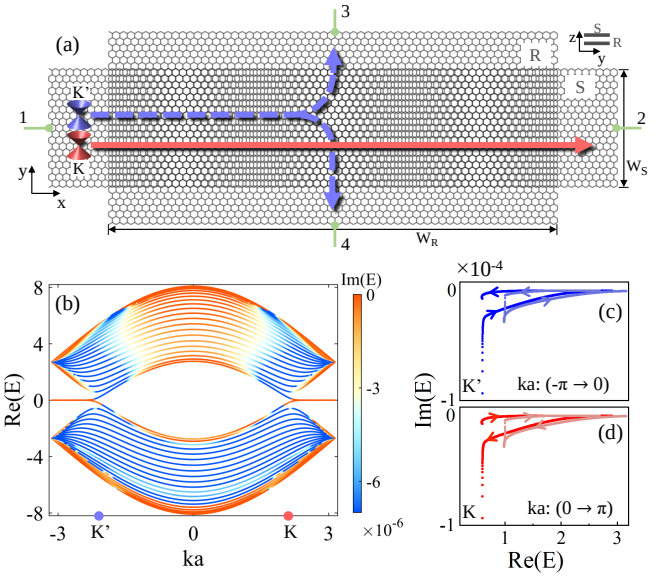

FIG. 1. (a) Schematic diagram of the proposed interface system composed of an upper graphene layer S and a lower graphene layer R, with four terminals labeled by 1-4. Electrons in the K valley can transmit from 1 to 2 while those in the K' valley are filtered out by entering the R layer. (b) The effective complex bands of S with the interlayer hopping strength set to one percent of its original value for better illustration. (c,d) Complex energy spectra of the two lowest sub-conduction bands (above the bands with zero energy) with the directions of spectral winding marked by arrows, which corresponds to the change of ka (c) from $-\pi$ to 0 and (d) from 0 to π, respectively. The relevant parameters are $a_0 = 0.142$ nm, $W_S = 29a_0$, $d_0 = 0.335$ nm, $t_\perp^0 = 0.48$ eV and $\delta_0 = 0.319a_0$.

other. The overlapping area of the two layers is $W_S \times W_R$. The bilayer system can be captured by the tight-binding Hamiltonian as

$$H = -t\sum_{\langle i,j\rangle} c_i^\dagger c_j - \sum_{i,j} t_\perp(\mathbf{r}_i,\mathbf{r}_j)c_i^\dagger c_j, \tag{1}$$

where $c_i^\dagger$ (c_i) creates (annihilates) electrons at site i. The first term describes the intralayer nearest-neighbor hopping with strength $t = 2.7$ eV, and the second term corresponds to the interlayer hopping [45–47]

$$t_\perp(\mathbf{r}_i,\mathbf{r}_j) = te^{-\frac{r-a_0}{\delta_0}}\left[1-(\mathbf{r}\cdot\hat{z}/r)^2\right] - t_\perp^0 e^{-\frac{r-d_0}{\delta_0}}(\mathbf{r}\cdot\hat{z}/r)^2. \tag{2}$$

Here, $\mathbf{r} = \mathbf{r}_i - \mathbf{r}_j$ is the displacement vector between two sites, $\hat{z}$ is the unit vector in the z-direction, a_0 is the intralayer site spacing, d_0 is the interlayer spacing, and $t_\perp^0 = 0.48$ eV is the vertical hopping between two layers according to the ab initio calculations [45]. The hopping decays exponentially within a typical scale δ_0.

The 1D moiré superlattice [48] can be achieved by including a uniaxial strain on the R layer in the x-direction. Accordingly, the scale of R layer is changed by a factor ε in the x-direction and the x-coordinate of the lattice sites changes through $x_i \to (1+\varepsilon)x_i$. It is assumed that the y-coordinate remains unchanged by neglecting the Poisson's ratio of graphene [49]. Such deformation of R gives rise to a moiré pattern in the x-direction; see Fig. 1(a). The main effect of the deformation of the R layer can be clearly seen in the momentum space, which drives the two Dirac points K, K' moving towards the Γ point in the projected 1D Brillouin zone [50]. As a result, a relative shift takes place between the Dirac cones in the two layers, which breaks the reciprocity within each valley. The moiré superlattice is assumed to be commensurate for simplicity such that $1+\varepsilon = m/n$ is a rational number with $m, n \in \mathbb{N}$. The primitive wavevectors of the S layer, R layer and the whole moiré superlattice are given by $\mathbf{b}_S = (2\pi/a)\hat{x}$, $\mathbf{b}_R = n\mathbf{b}_S/m$ and $\mathbf{b}_M = \mathbf{b}_S/m$, respectively, with $a = \sqrt{3}a_0$.

Complex energy bands.-Although the Hamiltonian (1) that describes the bilayer system is inherently Hermitian, our study instead concentrates on the non-Hermitian physics within the S layer, whose electronic property is engineered by the R layer [44]. It provides an important perspective for the understanding of the transport properties. Electrons in S can penetrate into R and finally escape into leads 3 and 4, thus undergoing an effective loss [cf. Fig. 1(a)]. The physics within S can be described by the Green's function in a general form as

$$g_S^r(\omega) = \left(\omega - H_S^{\text{eff}}\right)^{-1}, \quad H_S^{\text{eff}}(\omega) = H_S + \Sigma_R^r(\omega), \tag{3}$$

where the effective Hamiltonian H_S^{eff} consists of the bare Hamiltonian H_S of the S layer and the retarded self-energy $\Sigma_R^r(\omega)$, which is non-Hermitian. The self-energy is given by $\Sigma_R^r(\omega) = \hat{V}g_R^r(\omega)\hat{V}^\dagger$, where $\hat{V}$ is the interlayer hopping matrix and $g_R^r(\omega) = (\omega - H_R - \Sigma_3^r - \Sigma_4^r)^{-1}$ is the retarded Green's function of the R layer. Here, H_R is the Hamiltonian of the R layer and the effect of leads 3 and 4 is absorbed into the surface self-energy $\Sigma_{3,4}^r$, which is calculated using the iterative method [51].

The electron dynamics in S is governed by $H_S^{\text{eff}}(\omega)$, making it insightful to explore its complex energy bands. For this purpose, we first assume that both S and R layers extend to infinity in the x-direction. For the commensurate moiré modulation, the interlayer coupling takes place between the Bloch states with their wave vectors differing by a reciprocal superlattice vector $\mathbf{G}_\alpha = l\mathbf{b}_M$, where $\alpha = S, R$ is the layer index and $l \in \mathbb{Z}$. The Bloch Hamiltonian for the bilayer is expressed as

$$H(\mathbf{k}) = \sum_{\alpha,\beta=S,R}\sum_{\mathbf{G}_\alpha,\mathbf{G}'_\beta} c_{\mathbf{k}+\mathbf{G}_\alpha}^\dagger H_{\mathbf{G}_\alpha,\mathbf{G}'_\beta}(\mathbf{k})c_{\mathbf{k}+\mathbf{G}'_\beta}, \tag{4}$$

where the Bloch wave vector $\mathbf{k} \in [-\mathbf{b}_M/2, \mathbf{b}_M/2]$ lie in the moiré Brillouin zone and the summation over the reciprocal superlattice vector is restricted by the condition that the total wave vector $\mathbf{k} + \mathbf{G}_\alpha = \mathbf{q}_\alpha$ lies

in the first Brillouin zone of the α layer. As such, the reciprocal vectors $\{\mathbf{G}_\alpha\}$ become band labels and all bands are folded up into the moiré Brillouin zone. The Fermi annihilation operator is expressed by the sublattice components as $c_{\mathbf{q}_\alpha} = (c^1_{\mathbf{q}_\alpha}, c^2_{\mathbf{q}_\alpha}, \cdots, c^\chi_{\mathbf{q}_\alpha}, \cdots)^{\mathrm{T}}$ with $c^\chi_{\mathbf{q}_\alpha} = N_\alpha^{-1/2} \sum_{\mathbf{r}^\chi_\alpha} e^{i\mathbf{q}_\alpha \cdot \mathbf{r}^\chi_\alpha} c_{\mathbf{r}^\chi_\alpha}$, where the lattice site is specified by its location $\mathbf{r}^\chi_\alpha$ and N_α is the number of unit cells. The matrix elements in Eq. (4) are specified as follows. $H_{\mathbf{G}_S,\mathbf{G}'_S} = H_S(\mathbf{k}+\mathbf{G}_S)\delta_{\mathbf{G}_S,\mathbf{G}'_S}$ is diagonal in the $\mathbf{G}_S$ space with $H_S(\mathbf{k}+\mathbf{G}_S)$ the Bloch Hamiltonian of the S layer. Similarly, $H_{\mathbf{G}_R,\mathbf{G}'_R} = \tilde{H}_R(\mathbf{k}+\mathbf{G}_R)\delta_{\mathbf{G}_R,\mathbf{G}'_R}$ is diagonal in the $\mathbf{G}_R$ space with $\tilde{H}_R(\mathbf{k}+\mathbf{G}_R) = H_R(\mathbf{k}+\mathbf{G}_R) + \Sigma^r_3(\mathbf{k}+\mathbf{G}_R) + \Sigma^r_4(\mathbf{k}+\mathbf{G}_R)$ the effective Hamiltonian of the R layer composed of the bare Hamiltonian and the self-energies due to leads 3 and 4 [51]. Finally, the interlayer coupling matrix is calculated by $H_{\mathbf{G}_S,\mathbf{G}'_R} = H^\dagger_{\mathbf{G}'_R,\mathbf{G}_S} = \langle \Phi^S_{\mathbf{k}+\mathbf{G}_S} | \hat{V} | \Phi^R_{\mathbf{k}+\mathbf{G}'_R} \rangle$, in which $|\Phi^\alpha_{\mathbf{q}_\alpha}\rangle$ is the Bloch function of the α layer.

Integrating out the R layer following Eq. (3) yields the self-energy matrix $\Sigma^r_R(\omega, \mathbf{k}; \mathbf{G}_S, \mathbf{G}'_S) = \sum_{\mathbf{G}_R} H_{\mathbf{G}_S,\mathbf{G}_R}[\omega - \tilde{H}_R(\mathbf{k}+\mathbf{G}_R)]^{-1} H^\dagger_{\mathbf{G}'_S,\mathbf{G}_R}$. The complex band structures can be obtained by diagonalizing the effective Hamiltonian of the S layer $H^{\mathrm{eff}}_S(\omega, \mathbf{k}) = H_S + \Sigma^r_R$. Due to the folding of the complex bands, the information regarding the two valleys is hidden. To extract the valley flavor of the states, we unfold the multiple bands back to the original Brillouin zone of the S layer by tracking the momentum index $\mathbf{G}_S$ [52]. Futhermore, since the self-energy $\Sigma^r_R(\omega, \mathbf{k})$ is itself a function of energy ω, only the eigenvalues of $H^{\mathrm{eff}}_S(\omega, \mathbf{k})$ that fulfill $\mathrm{Re}[E(\mathbf{k})] = \omega$ have physical meanings and are considered. The complex band structure, shown in Fig. 1(b), highlights both the real and imaginary parts of the energy spectrum, for which the valley-resolved nonreciprocal transport can be clearly revealed. Specifically, the lifetime $\tau(\omega, \mathbf{k})$ of electrons in S is determined by $\tau^{-1} = -\mathrm{Im}[E(\omega, \mathbf{k})]$. From Fig. 1(b). It is observed that the right-moving electrons around the K valley possess a longer lifetime compared to the left-moving electrons within the same valley. The opposite situation applies to the K' valley as expected from time-reversal symmetry, thus exhibiting a valley-resolved nonreciprocity. Such scenario can be further illustrated by the complex spectral winding [40–43]. Here, we have separated the spectral winding for the two valleys depicted in Figs. 1(c) and 1(d), where the arrows represent the momentum increase. Note that only the two lowest sub-conduction bands are shown for clarity. The complex energy spectra in Figs. 1(c) and 1(d) are identical, but they exhibit opposite winding directions, indicating a valley-resolved non-Hermitian skin effect. The spectral winding, along with the distinct separation of the two valleys in the momentum space, indicates the robustness of this effect.

Non-Hermitian moiré valley filter.-The valley-resolved nonreciprocal transport can be utilized to create a novel type of valley filter. In contrast to previous proposals, the current scenario exploits a non-Hermitian strategy. We numerically study the electron transport between lead 1 and 2 through the moiré valley filter using the standard scattering matrix approach [53] based on the Hermitian Hamiltonian (1). To reveal the valley-resolved scattering, we label different transport channels with the wave vector $\mathbf{k}$ for a specific incident energy ω [51]. In particular, the amplitude $t_{\mathbf{k}_2,\mathbf{k}_1}(\omega)$ corresponds to the transmission from channel $\mathbf{k}_1$ in lead 1 into channel $\mathbf{k}_2$ in lead 2. Within the energy window of interest where the valley degree of freedom is well defined, electrons that lie in the K and K' valley can be selected by the conditions of $k \in [0, \pi/a]$ and $k \in [-\pi/a, 0]$, respectively [51].

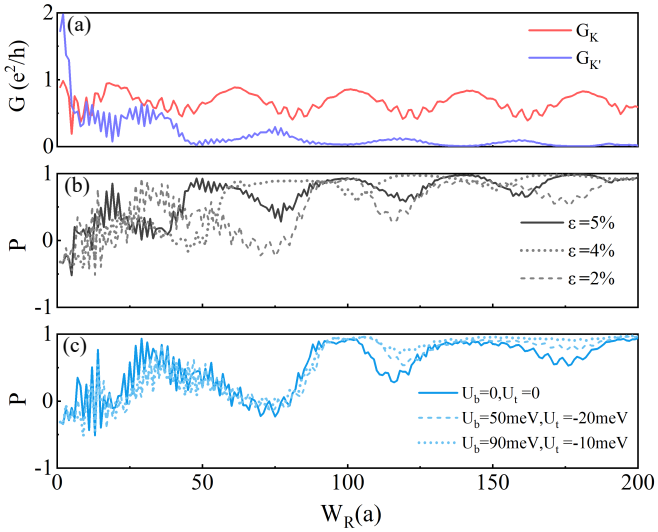

FIG. 2. (a) Valley-resolved differential conductance as a function of W_R with $\varepsilon = 5\%$. (b) Valley polarization with different distortion factors ε. (c) Valley polarization adjusted by the gate voltages with $\varepsilon = 2\%$. The bias voltage is $eV = 0.81$ eV and the other parameters are the same as those in Fig. 1.

By applying a bias voltage V on lead 1 and keeping the other three leads grounded, the differential conductance with the valley index $\kappa = K, K'$ is defined as

$$G_\kappa(eV) = \frac{e^2}{h} \sum_{\mathbf{k}_1} \sum_{\mathbf{k}_2 \in \kappa} |t_{\mathbf{k}_2,\mathbf{k}_1}|^2, \tag{5}$$

which is contributed by the transmitted electrons in the κ valley in lead 2, while the incident electrons from lead 1 occupy both valleys. The numerical results of G_K and $G_{K'}$ as a function of W_R are shown in Fig. 2(a). Because of the valley-resolved nonreciprocity, $G_{K'}$ decays much faster than G_K as W_R increases. Furthermore, both conductances exhibit additional oscillations arising from the intravalley interference.

The valley polarization of the current is quantified by [1]

$$P = \frac{G_K - G_{K'}}{G_K + G_{K'}}, \tag{6}$$

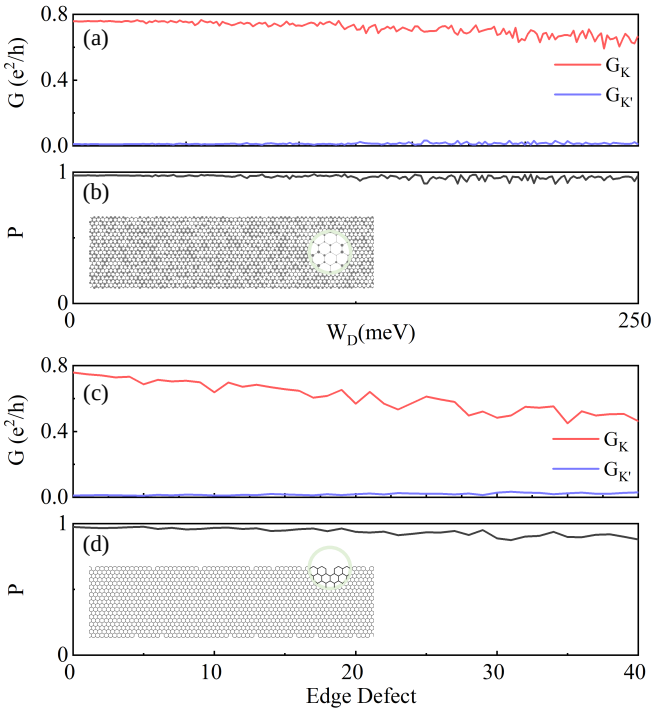

FIG. 3. Valley-resolved conductance and valley polarization as a function of (a,b) disorder strength and (c,d) number of edge defects. The relevant parameters are $\varepsilon = 5\%$, $W_R = 141a$, and the other parameters are the same as those in Fig. 1.

where $P > 0$ ($P < 0$) correspond to valley polarization at K (K'). The valley polarization corresponding to the conductance in Fig. 2(a) is depicted in Fig. 2(b) by the solid line. It can be observed that the current becomes K-valley polarized as W_R exceeds a certain value. Notably, a polarization of $P \simeq 100\%$ can be achieved around the plateaus. The results with different deformation factors ε are compared in Fig. 2(b), where the contrast in P that appears first for small W_R decreases and eventually disappears as W_R increases. A similar situation occurs for the setup with different widths W_S [51], indicating that the decrease of the valley polarization for a larger W_S can be compensated by a larger W_R. These results highlight the universality of our proposal. The positive valley polarization here underscores the main distinction between the current scenario and the one in Ref. [1]. For the latter, the presence of an additional right-moving mode at the K' valley in the conduction band would lead to a negative polarization with the same parameters.

The valley polarization can be further enhanced by applying gate voltages [54–58]. Their effects can be simulated by two on-site potential U_t and U_b in the respective layer as $H_g = \sum_{i\in S} U_t c_i^\dagger c_i + \sum_{i\in R} U_b c_i^\dagger c_i$. The impact of the gate voltages is illustrated in Fig. 2(c), which results in a suppression of the oscillation in P and effectively expands the parameter region with $P \simeq 100\%$. This property alleviates the stringent requirement for a specific W_R to achieve an efficient valley filter.

Robustness.-In contrast to previous proposals [1, 19–29], our scheme capitalizes on the non-Hermitian topological effect, making it more robust against various lattice imperfections. Consider an electron in the K valley incident from lead 1. It may be scattered to the K' valley, either with or without changing its propagating direction. In the case of inter-valley forward scattering, the electron rapidly decays into the R layer and exhibits a short lifetime, as shown in Fig. 1(b), preventing it from reaching lead 2. As for the inter-valley backward scattering, the electron is reflected back into lead 1. Therefore, both two processes of inter-valley scattering do not contribute to the output current in lead 2, and so leave the valley polarization unaffected.

Here, we examine two types of imperfections commonly encountered in the system: local disorder and edge defects. We first consider the effect of Anderson disorder depicted by the inset of Fig. 3(b). It is described by the random on-site potential $H_{\rm dis} = \sum_{i\in S} U_i c_i^\dagger c_i$ in the S layer, where $U_i \in [-W_D/2, W_D/2]$ with W_D the disorder strength. The valley-resolved transport is shown in Figs. 3(a) and 3(b), in which the high valley polarization persists despite the disorder of a moderate strength. Moving on to the edge defects, we consider vacancies that randomly exist at the zigzag edges of the S layer; refer to the inset of Fig. 3(d). Similar to the disorder effect, the valley polarization remains high even in the presence of a large number of edge defects as shown in Figs. 3(c) and 3(d). Moreover, the impact of edge defects is expected to diminish as the width W_S increases because the valley filter relies primarily on bulk transport.

During the fabrication a small twist between the two layers can appear accidentally. This is simulated by a rotation of the R layer and consequently, the interlayer hopping changes its magnitude according to Eq. (2) by using the twisted geometry. By calculating the conductance $G_{K,K'}$ and valley polarization P as a function of the twist angle, we find that the valley polarization is always positive and exhibits an interesting oscillation behavior. Furthermore, nearly perfect valley polarization can be realized around different plateaus; see Supplemental Material [51] for more details.

Discussion and outlook.-We have demonstrated an efficient strategy to create a valley filter in a heterostrained graphene bilayer stemming from the moiré modulation. The valley filter effect relies on the 1D moiré pattern, which can be realized by a differential and uniaxial strain [59, 60]. The underlying non-Hermitian topological scenario guarantees its robustness against lattice imperfections, lifting the stringent implementation requirements of previous proposals. The universality of the mechanism implies that the reduction of nonreciprocity due to increased W_S can be compensated by using a larger W_R. Moreover, the device with a larger scale effectively reduces the energy spacing between transverse

modes and so a small bias voltage is sufficient to drive the valley-resolved transport. Compared with previous proposals using valley polarized edge transport [61–63], our scheme can generate a larger valley current and can be directly applied to construct valleytronic devices, such as the valley valve. Due to the bulk origin of our mechanism, the impact of irregular edges becomes negligible for wide devices. Our moiré valley filter mechanism can be readily extended to other hexagonal 2D materials, including transition metal dichalcogenides [3, 4], where the spin-valley locking effect can further enhance the robustness of the valley filter against nonmagnetic disorders [64]. Furthermore, a similar strategy can be applied to create the valley-resolved non-Hermitian skin effect in metamaterials, such as photonic and phononic crystals [65–69]. Our results pave the way for exploring the valley-resolved non-Hermitian skin effect, establishing an overlooked connection between non-Hermiticity and moiré physics [70–75].

This work was supported by the National Key Projects for Research and Development of China under Grant No. 2022YFA120470 (W.C.), the National Natural Science Foundation of China under Grant No. 12074172 (W.C.), No. 12222406 (W.C.) and No. 12174182 (D.Y.X.), and the State Key Program for Basic Researches of China under Grants No. 2021YFA1400403 (D.Y.X.). J.L.L acknowledges the support from Aalto Science-IT project, the Academy of Finland Projects No. 331342, No. 336243 and No. 358088, and the Jane and Aatos Erkko Foundation.

* Corresponding author: pchenweis@gmail.com

[1] A. Rycerz, J. Tworzydło, and C. Beenakker, Nature Physics **3**, 172 (2007).
[2] X. Xu, W. Yao, D. Xiao, and T. F. Heinz, Nature Physics **10**, 343 (2014).
[3] J. R. Schaibley, H. Yu, G. Clark, P. Rivera, J. S. Ross, K. L. Seyler, W. Yao, and X. Xu, Nature Reviews Materials **1**, 1 (2016).
[4] S. A. Vitale, D. Nezich, J. O. Varghese, P. Kim, N. Gedik, P. Jarillo-Herrero, D. Xiao, and M. Rothschild, Small **14**, 1801483 (2018).
[5] I. Žutić, J. Fabian, and S. D. Sarma, Reviews of modern physics **76**, 323 (2004).
[6] D. Xiao, W. Yao, and Q. Niu, Physical review letters **99**, 236809 (2007).
[7] M. Yamamoto, Y. Shimazaki, I. V. Borzenets, and S. Tarucha, Journal of the Physical Society of Japan **84**, 121006 (2015).
[8] R. Gorbachev, J. Song, G. Yu, A. Kretinin, F. Withers, Y. Cao, A. Mishchenko, I. Grigorieva, K. S. Novoselov, L. Levitov, *et al.*, Science **346**, 448 (2014).
[9] K. F. Mak, K. L. McGill, J. Park, and P. L. McEuen, Science **344**, 1489 (2014).
[10] K. F. Mak, K. He, J. Shan, and T. F. Heinz, Nature nanotechnology **7**, 494 (2012).
[11] H. Zeng, J. Dai, W. Yao, D. Xiao, and X. Cui, Nature nanotechnology **7**, 490 (2012).
[12] T. Cao, G. Wang, W. Han, H. Ye, C. Zhu, J. Shi, Q. Niu, P. Tan, E. Wang, B. Liu, *et al.*, Nature communications **3**, 887 (2012).
[13] A. M. Jones, H. Yu, N. J. Ghimire, S. Wu, G. Aivazian, J. S. Ross, B. Zhao, J. Yan, D. G. Mandrus, D. Xiao, *et al.*, Nature nanotechnology **8**, 634 (2013).
[14] A. Srivastava, M. Sidler, A. V. Allain, D. S. Lembke, A. Kis, and A. Imamoğlu, Nature Physics **11**, 141 (2015).
[15] G. Aivazian, Z. Gong, A. M. Jones, R.-L. Chu, J. Yan, D. G. Mandrus, C. Zhang, D. Cobden, W. Yao, and X. Xu, Nature Physics **11**, 148 (2015).
[16] Y. Li, J. Ludwig, T. Low, A. Chernikov, X. Cui, G. Arefe, Y. D. Kim, A. M. van der Zande, A. Rigosi, H. M. Hill, S. H. Kim, J. Hone, Z. Li, D. Smirnov, and T. F. Heinz, Phys. Rev. Lett. **113**, 266804 (2014).
[17] D. MacNeill, C. Heikes, K. F. Mak, Z. Anderson, A. Kormányos, V. Zólyomi, J. Park, and D. C. Ralph, Phys. Rev. Lett. **114**, 037401 (2015).
[18] A. V. Stier, K. M. McCreary, B. T. Jonker, J. Kono, and S. A. Crooker, Nature communications **7**, 10643 (2016).
[19] D. Gunlycke and C. T. White, Phys. Rev. Lett. **106**, 136806 (2011).
[20] Y. Liu, J. Song, Y. Li, Y. Liu, and Q.-f. Sun, Phys. Rev. B **87**, 195445 (2013).
[21] J.-H. Chen, G. Autès, N. Alem, F. Gargiulo, A. Gautam, M. Linck, C. Kisielowski, O. V. Yazyev, S. G. Louie, and A. Zettl, Phys. Rev. B **89**, 121407 (2014).
[22] I. Martin, Y. M. Blanter, and A. F. Morpurgo, Phys. Rev. Lett. **100**, 036804 (2008).
[23] Z. Qiao, J. Jung, C. Lin, Y. Ren, A. H. MacDonald, and Q. Niu, Phys. Rev. Lett. **112**, 206601 (2014).
[24] Z. Qiao, J. Jung, Q. Niu, and A. H. MacDonald, Nano letters **11**, 3453 (2011).
[25] J. Li, R.-X. Zhang, Z. Yin, J. Zhang, K. Watanabe, T. Taniguchi, C. Liu, and J. Zhu, Science **362**, 1149 (2018).
[26] T. Fujita, M. Jalil, and S. Tan, Applied Physics Letters **97**, 043508 (2010).
[27] Y. Jiang, T. Low, K. Chang, M. I. Katsnelson, and F. Guinea, Phys. Rev. Lett. **110**, 046601 (2013).
[28] F. Zhai, Y. Ma, and K. Chang, New Journal of Physics **13**, 083029 (2011).
[29] M. Settnes, S. R. Power, M. Brandbyge, and A.-P. Jauho, Phys. Rev. Lett. **117**, 276801 (2016).
[30] S. M. Girvin and K. Yang, *Modern condensed matter physics* (Cambridge University Press, 2019).
[31] J. Y. Lee, J. Ahn, H. Zhou, and A. Vishwanath, Phys. Rev. Lett. **123**, 206404 (2019).
[32] T. Bessho and M. Sato, Phys. Rev. Lett. **127**, 196404 (2021).
[33] W.-Q. Chen, Y.-S. Wu, W. Xi, W.-Z. Yi, and G. Yue, Journal of High Energy Physics **2023**, 1 (2023).
[34] S. Yao and Z. Wang, Phys. Rev. Lett. **121**, 086803 (2018).
[35] S. Yao, F. Song, and Z. Wang, Phys. Rev. Lett. **121**, 136802 (2018).
[36] F. K. Kunst, E. Edvardsson, J. C. Budich, and E. J. Bergholtz, Phys. Rev. Lett. **121**, 026808 (2018).
[37] K. Yokomizo and S. Murakami, Phys. Rev. Lett. **123**, 066404 (2019).
[38] Z. Yang, K. Zhang, C. Fang, and J. Hu, Phys. Rev. Lett. **125**, 226402 (2020).
[39] K. Shao, Z.-T. Cai, H. Geng, W. Chen, and D. Y. Xing, Phys. Rev. B **106**, L081402 (2022).

[40] D. S. Borgnia, A. J. Kruchkov, and R.-J. Slager, Phys. Rev. Lett. **124**, 056802 (2020).

[41] N. Okuma, K. Kawabata, K. Shiozaki, and M. Sato, Phys. Rev. Lett. **124**, 086801 (2020).

[42] K. Zhang, Z. Yang, and C. Fang, Phys. Rev. Lett. **125**, 126402 (2020).

[43] E. J. Bergholtz, J. C. Budich, and F. K. Kunst, Rev. Mod. Phys. **93**, 015005 (2021).

[44] H. Geng, J. Y. Wei, M. H. Zou, L. Sheng, W. Chen, and D. Y. Xing, Phys. Rev. B **107**, 035306 (2023).

[45] G. Trambly de Laissardière, D. Mayou, and L. Magaud, Nano letters **10**, 804 (2010).

[46] S. Uryu, Phys. Rev. B **69**, 075402 (2004).

[47] T. Nakanishi and T. Ando, Journal of the Physical Society of Japan **70**, 1647 (2001).

[48] A. Timmel and E. J. Mele, Phys. Rev. Lett. **125**, 166803 (2020).

[49] V. M. Pereira, A. H. Castro Neto, and N. M. R. Peres, Phys. Rev. B **80**, 045401 (2009).

[50] The deformation of the R layer slightly changes the intralayer nearest-neighbor hopping as well. This modification of intralayer hopping is also governed by Eq. (2), but its impact is negligible.

[51] See Supplemental Material at xxxx for the calculation of self-energies due to leads, derivation of the Bloch Hamiltonian for the bilayer system, numerical calculation of the transmission coefficients, valley polarization for different W_S, and the effect due to small twist, which includes Refs. [53, 76–80].

[52] During the band-folding process, one can establish a correspondence between the band index n in the moiré Brillouin zone and the momentum shift $\mathbf{G}_S^n = n\mathbf{b}_M$ of the state in the original Brillouin zone of S, where n is an integer. Band unfolding can be understood as the inverse process [81–83]. When coupling between different bands occurs in the moiré Brillouin zone, we solve the eigenstates and identify the component n' with the highest weight and unfold the band through $E_{n'}(\mathbf{k}) = E(\mathbf{k} + \mathbf{G}_S^{n'})$. The complete band unfolding is achieved by repeating this procedure for all bands in the moiré Brillouin zone. By doing so, the valley-associated information, initially smeared in the moiré Brillouin zone, is recovered.

[53] S. Datta, *Electronic transport in mesoscopic systems* (Cambridge university press, 1997).

[54] J. B. Oostinga, H. B. Heersche, X. Liu, A. F. Morpurgo, and L. M. Vandersypen, Nature materials **7**, 151 (2008).

[55] E. V. Castro, K. S. Novoselov, S. V. Morozov, N. M. R. Peres, J. M. B. L. dos Santos, J. Nilsson, F. Guinea, A. K. Geim, and A. H. C. Neto, Phys. Rev. Lett. **99**, 216802 (2007).

[56] H. Chen, P. Zhou, J. Liu, J. Qiao, B. Oezyilmaz, and J. Martin, Nature communications **11**, 1202 (2020).

[57] M. Sui, G. Chen, L. Ma, W.-Y. Shan, D. Tian, K. Watanabe, T. Taniguchi, X. Jin, W. Yao, D. Xiao, *et al.*, Nature Physics **11**, 1027 (2015).

[58] Y. Shimazaki, M. Yamamoto, I. V. Borzenets, K. Watanabe, T. Taniguchi, and S. Tarucha, Nature Physics **11**, 1032 (2015).

[59] C. Si, Z. Sun, and F. Liu, Nanoscale **8**, 3207 (2016).

[60] Y. Bai, L. Zhou, J. Wang, W. Wu, L. J. McGilly, D. Halbertal, C. F. B. Lo, F. Liu, J. Ardelean, P. Rivera, *et al.*, Nature Materials **19**, 1068 (2020).

[61] H. Pan, Z. Li, C.-C. Liu, G. Zhu, Z. Qiao, and Y. Yao, Phys. Rev. Lett. **112**, 106802 (2014).

[62] H. Pan, X. Li, F. Zhang, and S. A. Yang, Phys. Rev. B **92**, 041404 (2015).

[63] T. Zhou, J. Zhang, Y. Xue, B. Zhao, H. Zhang, H. Jiang, and Z. Yang, Phys. Rev. B **94**, 235449 (2016).

[64] T. Zhou, S. Cheng, M. Schleenvoigt, P. Schüffelgen, H. Jiang, Z. Yang, and I. Žutić, Phys. Rev. Lett. **127**, 116402 (2021).

[65] S. Weidemann, M. Kremer, T. Helbig, T. Hofmann, A. Stegmaier, M. Greiter, R. Thomale, and A. Szameit, Science **368**, 311 (2020).

[66] A. Ghatak, M. Brandenbourger, J. Van Wezel, and C. Coulais, Proceedings of the National Academy of Sciences **117**, 29561 (2020).

[67] X. Zhang, Y. Tian, J.-H. Jiang, M.-H. Lu, and Y.-F. Chen, Nature communications **12**, 5377 (2021).

[68] L. Zhang, Y. Yang, Y. Ge, Y.-J. Guan, Q. Chen, Q. Yan, F. Chen, R. Xi, Y. Li, D. Jia, *et al.*, Nature communications **12**, 6297 (2021).

[69] Q. Zhou, J. Wu, Z. Pu, J. Lu, X. Huang, W. Deng, M. Ke, and Z. Liu, Nature Communications **14**, 4569 (2023).

[70] E. Y. Andrei and A. H. MacDonald, Nature materials **19**, 1265 (2020).

[71] L. Balents, C. R. Dean, D. K. Efetov, and A. F. Young, Nature Physics **16**, 725 (2020).

[72] E. Y. Andrei, D. K. Efetov, P. Jarillo-Herrero, A. H. MacDonald, K. F. Mak, T. Senthil, E. Tutuc, A. Yazdani, and A. F. Young, Nature Reviews Materials **6**, 201 (2021).

[73] D. M. Kennes, M. Claassen, L. Xian, A. Georges, A. J. Millis, J. Hone, C. R. Dean, D. Basov, A. N. Pasupathy, and A. Rubio, Nature Physics **17**, 155 (2021).

[74] C. N. Lau, M. W. Bockrath, K. F. Mak, and F. Zhang, Nature **602**, 41 (2022).

[75] K. F. Mak and J. Shan, Nature Nanotechnology **17**, 686 (2022).

[76] M. B. Nardelli, Phys. Rev. B **60**, 7828 (1999).

[77] M. P. L. Sancho, J. M. L. Sancho, J. M. L. Sancho, and J. Rubio, Journal of Physics F: Metal Physics **15**, 851 (1985).

[78] T. Ando, Phys. Rev. B **44**, 8017 (1991).

[79] K. Wakabayashi, *Low-Energy Physical Properties of Edge States in Nano-Graphites*, Ph.D. thesis, University of Tsukuba (2000).

[80] P. A. Khomyakov, G. Brocks, V. Karpan, M. Zwierzycki, and P. J. Kelly, Phys. Rev. B **72**, 035450 (2005).

[81] T. B. Boykin and G. Klimeck, Phys. Rev. B **71**, 115215 (2005).

[82] V. Popescu and A. Zunger, Phys. Rev. Lett. **104**, 236403 (2010).

[83] P. V. C. Medeiros, S. Stafström, and J. Björk, Phys. Rev. B **89**, 041407 (2014).